Atmos. Chem. Phys. Discuss., 15, 22597–22636, 2015
www.atmos-chem-phys-discuss.net/15/22597/2015/
doi:10.5194/acpd-15-22597-2015

Atmospheric Chemistry and Physics Discussions

New insight into the spatiotemporal variability and source apportionments of C_1–C_4 alkyl nitrates in Hong Kong

Z. H. Ling[1,2], H. Guo[2], I. J. Simpson[3], S. M. Saunders[4], S. H. M. Lam[4,5], X. P. Lyu[2], and D. R. Blake[3]

[1]Department of Atmospheric Sciences, School of Environmental Science and Engineering, Sun Yat-sen University, Guangzhou, China
[2]Air Quality Studies, Department of Civil and Environmental Engineering, The Hong Kong Polytechnic University, Hong Kong
[3]Department of Chemistry, University of California, Irvine, CA, USA
[4]School of Chemistry and Biochemistry, University of Western Australia, Perth, Western Australia, Australia
[5]Pacific Environment Limited, Perth, Western Australia, Australia

Received: 22 June 2015 – Accepted: 2 August 2015 – Published: 24 August 2015

Correspondence to: H. Guo (ceguohai@polyu.edu.hk)

Published by Copernicus Publications on behalf of the European Geosciences Union.

Abstract

Alkyl nitrates ($RONO_2$) were measured concurrently at a mountain site (TMS) and an urban site (TW) at the foot of the same mountain in Hong Kong from September to November 2010, when high O_3 mixing ratios were frequently observed. The abundance and temporal patterns of five C_1–C_4 $RONO_2$ and their parent hydrocarbons (RH), the $RONO_2$/RH ratios and photochemical age of air masses at TMS differed from those at TW, reflecting different contributions of direct emissions and secondary formation of $RONO_2$ at the two sites. Relative to 2-$BuONO_2$/*n*-butane, the measured ratios of C_1–C_2 $RONO_2$/RH at the two sites exhibited significant positive deviations from pure photochemical (PP) curves and background initial ratio (BIR) curves obtained from laboratory kinetic data, suggesting that background mixing ratios had a significant influence on the $RONO_2$ and RH distributions. In contrast to the C_1–C_2 $RONO_2$/RH ratios, the evolution for the measured ratios of C_3 $RONO_2$/RH to 2-$BuONO_2$/*n*-butane agreed well with the ratio distributions in the PP and BIR curves at the two sites. Furthermore, the ratios of 1-/2-$PrONO_2$ and yields of 1- and 2-$PrONO_2$ suggested that the C_3 $RONO_2$ were mainly from secondary formation at TMS, whereas secondary formation and other additional sources had a significant influence on C_3 $RONO_2$ mixing ratios at TW. The source apportionment results confirmed that secondary formation was the dominant contributor to all the $RONO_2$ at TMS, while most of the $RONO_2$ at TW were from secondary formation and biomass burning. The findings of the source apportionments and photochemical evolution of $RONO_2$ are helpful to evaluate photochemical processing in Hong Kong using $RONO_2$ as an indicator.

1 Introduction

Alkyl nitrates ($RONO_2$) are important photochemical pollutants in the atmosphere due to their roles in local, regional and global atmospheric chemistry (Atlas, 1988; Jenkin et al., 2000; Seinfeld and Pandis, 2006). $RONO_2$ are reactive nitrogen compounds

ACPD
15, 22597–22636, 2015

(NO_y) and act as a critical reservoir of nitrogen oxides ($NO_x = NO + NO_2$) during long-range transport due to their relatively low reactivity (Atkinson, 2006).

A number of studies conducted in different environments have shown that marine emissions emit $RONO_2$ directly and that $RONO_2$ is also produced indirectly through photochemical reactions (Roberts, 1990; Roberts et al., 1998; Blake et al., 2003; Simpson et al., 2002, 2003, 2006; Rosen et al., 2004; Reeves et al., 2007; Wang et al., 2013). In the case of biomass burning, secondary $RONO_2$ formation is believed to occur by the photo-oxidation of emitted hydrocarbons with a formation mechanism of RO and NO_2 (Simpson et al., 2002). The photochemical pathways for the secondary formation of $RONO_2$ are expressed as follows (Atkinson et al., 1982, 2006; Jenkin et al., 2000; Arey et al., 2001; Simpson et al., 2002; Sommariva et al., 2008):

$$RH + OH\cdot \rightarrow R\cdot + H_2O, k_1, \alpha_1 \quad \text{(R1)}$$

$$R\cdot + O_3 \rightarrow RO_2\cdot, k_2 \quad \text{(R2)}$$

$$RO_2\cdot + NO \rightarrow RO\cdot + NO_2, k_3, 1 - \alpha_2, \quad \text{(R3)}$$

$$RO_2\cdot + NO \rightarrow RONO_2, k_4, \alpha_2, \quad \text{(R4)}$$

$$RO + NO_2 \rightarrow RONO_2, k_5 \quad \text{(R5)}$$

where k_1, k_2, k_3, k_4 and k_5 are reaction rate constants. α_1 and α_2 are branching ratios for the corresponding radicals, which increase as the carbon number increases and are dependent on the carbon chain length.

Photochemical $RONO_2$ formation can influence the oxidation of NO to NO_2, subsequently leading to O_3 production by NO_2 photolysis. Therefore, $RONO_2$ can be used as indicators of photochemical O_3 production (Simpson et al., 2006). Furthermore, the interactions of $RONO_2$ with their parent hydrocarbons provide useful information about the photochemical processing of air masses. Comparing measured and predicted $RONO_2$/RH ratios calculated using the laboratory kinetic data as a function of time, Bertman et al. (1995) firstly examined the photochemical evolution of $RONO_2$ at Scotia, Pennsylvania and the Kinterbish Wildlife Area, Alabama, USA. Since then, this approach has been used to investigate the evolution of $RONO_2$ with air mass age in

ACPD
15, 22597–22636, 2015

different regions (Simpson et al., 2006; Reeves et al., 2007; Russo et al., 2010; Worton et al., 2010; Wang et al., 2013). Fairly good agreement (> 50 %) between measured and modeled ratios suggests that the oxidation of single-parent hydrocarbons represents the evolution of their daughter $RONO_2$. A measured ratio higher than the modeled line implies the possible influence of additional sources for C_1–C_5 $RONO_2$ other than the oxidation of their parent hydrocarbons, and measured ratios of C_2 $RONO_2$ lower than the modeled values probably result from the fragmentation of *n*-pentane to smaller chain peroxy radicals other than the 2-pentyl and 3-pentyl radicals (Reeves et al., 2007; Worton et al., 2010).

The main sinks for ambient $RONO_2$ are photolysis and reactions with hydroxyl radical (OH), making $RONO_2$ lifetimes vary with season, latitude and altitude (days to weeks):

$$RONO_2 + h\nu \rightarrow RO\cdot + NO_2, J_{RONO_2}, \quad \text{(R6)}$$

$$RONO_2 + OH\cdot \rightarrow \text{products}, k_6, \quad \text{(R7)}$$

where $h\nu$ is sunlight and J_{RONO_2} and k_6 are the photolysis and OH reaction rate constants, respectively. The importance of $RONO_2$ removal by photolysis decreases as the carbon number increases (Clemitshaw et al., 1997; Talukdar et al., 1997). Dry deposition has recently been recognized as another pathway for the removal of atmospheric $RONO_2$ (Russo et al., 2010; Wu et al., 2011).

Despite increased concern over photochemical pollution in Hong Kong and the greater Pearl River Delta (PRD) region, limited studies have focused on the characteristics of $RONO_2$, which share a common mechanism with photochemical O_3 formation and act as indicators of photochemical processing. For example, based on measurements taken in 2001–2002, Simpson et al. (2006) analyzed the general characteristics of $RONO_2$, i.e., levels and seasonal variations, at a coastal site (Tai O) in Hong Kong in 2001–2002. C_2–C_4 $RONO_2$ were the most abundant species, with maximum and minimum levels in winter and summer, respectively. The diurnal variations suggested that photochemical production was the dominant $RONO_2$ source at Tai O, a coastal village near Hong Kong. Furthermore, through approximate calculations, it was concluded that

ACPD
15, 22597–22636, 2015

the methoxy radical ($CH_3O\cdot$) reaction with NO_2 was a viable alternative pathway for the observed high levels of $MeONO_2$ during pollution episodes. This mechanism was subsequently verified by Archibald et al. (2007) via box model simulations, whereby R5 became important for $MeONO_2$ formation at 10 ppb NO_2 and dominant at 35 ppb NO_2. However, knowledge related to the chemical evolution and source apportionments of individual $RONO_2$ and their relationship with parent hydrocarbons is still lacking in Hong Kong, especially given that levels of $RONO_2$ precursors have varied since at least 2002 (Ling et al., 2014). Hence, in this study, intensive field measurements of C_1–C_4 $RONO_2$ were conducted at two sites, i.e., a mountain site (Mt. Tai Mo Shan, TMS) and an urban site (Tsuen Wan, TW) at the foot of the same mountain in Hong Kong, and the data were analyzed and compared with the previous study conducted at Tai O (Simpson et al., 2006). The aims were to investigate the spatiotemporal variations and, for the first time, source apportionments and photochemical evolution of $RONO_2$ in Hong Kong.

2 Methodology

2.1 Sampling sites

In this study, concurrent field measurements were conducted at two sites located at different elevations of the highest mountain in Hong Kong, i.e., Mt. Tai Mo Shan (TMS, elevation 967 m), from 6 September to 29 November 2010. A detailed description of the topography of Mt. TMS was provided in an overview paper (Guo et al., 2013a). In brief, Fig. 1 presents the two sampling locations and the surroundings. The high-elevation site (TMS) was set on the rooftop of a building at the waist of the mountain (640 m a.s.l.), the highest logistically feasible observation location, beyond which the area comprised natural territory with shrubs and grasses to the mountain summit (AFCD, 2015). The measurement site at the foot of the mountain was the monitoring station of the Hong Kong Environmental Protection Department (HKEPD) at Tsuen Wan (TW), a mixed

ACPD
15, 22597–22636, 2015

residential, commercial and light industrial area in the New Territories of Hong Kong. The TW monitoring site was located on the rooftop of a building, approximately 15–20 m a.g.l. The linear distance between the TMS and TW sites was about 7 km and the difference in elevation between the two sites was 630 m. In general, the solar radiation was comparable at the two sites, and the temperature was higher and the relative humidity and wind speed were lower at the TW site (Guo et al., 2013a). The winds at TMS were generally from the north with speeds ranging from 0.02 to 4 m s^{-1}, and the winds at TW were predominantly from the southeast at speeds of 1–3 m s^{-1} with easterly winds at night and southerly winds during the day. Due to its unique topography, the air at TMS was often influenced by the mountain-valley breezes and regional transport (Guo et al., 2013a). Based on the average wind speed and distance, the air parcel from upwind locations, i.e., the mountain foot at a local scale and/or inland PRD at a regional scale, took about 0. 6–1.6 h to arrive at the TMS site (Guo et al., 2012, 2013a).

2.2 Sampling and analysis of volatile organic compounds (VOCs)

Sixty-minute integrated VOC samples were collected on 10 O_3 episode days and 10 non-O_3 episode days using evacuated 2 L stainless steel canisters, and subjected to laboratory analysis at the University of California, Irvine (UCI). A total of 384 samples were collected at the two sites. The O_3 episode days were selected as the days with the highest daytime hourly O_3 level at a regional scale (higher than 100 ppbv), which were forecasted based on weather parameters and meteorological data analysis, and subsequently confirmed by the observed O_3 mixing ratios. During non-O_3 episode days, the hourly samples were collected from 07:00 to 19:00 local time (LT) at a sampling interval of 2 h (a total of 7 samples per day). On O_3 episode days, the hourly samples were consecutively collected from 09:00 to 16:00 LT with additional hourly samples collected at 18:00, 21:00, 00:00, 03:00 and 07:00 LT (a total of 13 samples per day). After the campaign, the VOC samples were delivered to UCI for chemical analysis. Other studies have provided detailed descriptions of the analytical system and the quality con-

ACPD
15, 22597–22636, 2015

trol, detection limits and analysis precision of the VOC samples (Colman et al., 2001; Simpson et al., 2006, 2010). In brief, the precision and detection limit of the $RONO_2$ measurements is 5 % and 0.02 pptv, respectively. The calibration scale for the $RONO_2$ measurements changed in 2008, increasing by factors of 2.13, 1.81, 1.24 and 1.17 for the C_2, C_2, C_2 and C_2 $RONO_2$, respectively (Simpson et al., 2011). In other words the $RONO_2$ data reported at Tai O by Simpson et al. (2006) were low compared with the data reported here, and the Tai O data have been adjusted to the new calibration scale to allow for direct comparison with this work.

2.3 Continuous measurements of O_3, CO and NO-NO_2-NO_x

At TMS, trace gases of O_3, CO and NO-NO_2-NO_x were measured using commercial analyzers with regular internal calibration with NIST (National Institute of Standards and Technology) traceable standards. O_3 was measured using a commercial UV photometric instrument (Advanced Pollution Instrumentation (API), model 400E) that had a detection limit of 0.6 ppbv. CO was measured with a gas filter correlation, nondispersive infrared analyzer (API, Model 300E) with a heated catalytic scrubber (as purchased) to convert CO to carbon dioxide (CO_2) for baseline determination. The detection limit was 30 ppbv for a 2 min average. The 2 s precision was about 1 % for a level of 500 ppbv (2 min average) and the overall uncertainty was estimated to be 10 %. NO, NO_2 and NO_x were detected with a chemiluminescence NO-NO_2-NO_x analyzer (API, Model 200E) that had a detection limit of 0.5 ppbv. For O_3, CO, NO and NO_x analyzer, a data logger (Environmental Systems Corporation Model 8816) was used to control the calibrations and to collect data, which were averaged to 1 min values.

In addition to the above chemical measurements, several meteorological parameters, including wind speeds and direction, temperature, relative humidity and solar radiation, were measured by the integrated sensor suite (Vantage Pro TM & Vantage Pro 2 Plus TM Weather Stations, Davis Instruments).

At TW, hourly data of O_3, CO, NO-NO_2-NO_x and meteorological parameters were obtained from the HKEPD (http://epic.epd.gov.hk/ca/uid/airdata). Detailed information

ACPD
15, 22597–22636, 2015

about the measurements, quality assurance and control protocols can be found in the HKEPD report (HKEPD, 2012).

2.4 Positive Matrix Factorization (PMF) model

In this study, PMF v3.0 was used for the source apportionments of the observed $RONO_2$ at TMS and TW. Our previous studies provided detailed information about the PMF model (Ling et al., 2011, 2014). In terms of the PMF input, the uncertainty for each species was determined as the sum of 10 % of the VOC concentration and two times the method detection limit (MDL) of the species (Paatero, 2000). Tracers for different sources were selected for the model input. For example, CO, ethane and ethyne were used as tracers for the combustion processes, and CH_3Cl was used to specifically indicate biomass burning (as opposed to fossil fuel combustion). DMS was a typical tracer for marine emissions, and O_x ($= O_3 + NO_2$) was used as the tracer for secondary formation through photochemical reactions. O_x also indicates photochemical $RONO_2$ formation because O_3, which can be titrated by NO and form NO_2, shares a common photochemical source with $RONO_2$ (Simpson et al., 2006). In addition to the aforementioned species, $RONO_2$ precursors, i.e., methane, propane and n/i-butanes, were input into the model. Sixteen compounds were used for the model input. Different checks and sensitivity tests, including the selection of factor solutions; the correlation between the observed and predicted concentrations of VOCs and $RONO_2$; the scale residuals, i.e., uncertainty over the different runs for the input species; and the bootstrap simulation results demonstrated that the performance of the model simulation was acceptable (Ling et al., 2011, 2014).

ACPD
15, 22597–22636, 2015

3 Results and discussion

3.1 General characteristics

3.1.1 Spatial variations

Table 1 presents the general features of $RONO_2$ and their parent hydrocarbons at TMS and TW. Figure 2 compares the $RONO_2$ levels measured at TMS and TW with those measured in different environments in previous studies. The levels of $MeONO_2$, $EtONO_2$ and 2-$PrONO_2$ were slightly higher at TW than at TMS ($p < 0.05$), with average values of 12.6±0.5 (mean ±95 % confidence interval), 13.3±0.6 and 26.3±1.2 pptv, respectively, at TW. The average mixing ratios of 1-$PrONO_2$ and 2-$BuONO_2$ were comparable at the two sites ($p > 0.05$). However, the TMS site was 630 m higher than the TW site, and the levels of parent *n*-alkanes at TMS were lower than at TW, suggesting different contributions of direct emissions, secondary formation and redistribution due to mesoscale circulations and regional transport at the two sites. Among all of the $RONO_2$, 2-$PrONO_2$ and 2-$BuONO_2$ were the most abundant at the two sites, consistent with the results observed in different environments (Blake et al., 2003; Simpson et al., 2006; Russo et al., 2010; Wang et al., 2013). The relatively higher levels of 2-$PrONO_2$ and 2-$BuONO_2$ were expected due to the balance of increased branching ratios for photochemical $RONO_2$ formation and the decreased lifetime of both parent alkanes and $RONO_2$ with increasing carbon numbers (Arey et al., 2001; Simpson et al., 2006; Russo et al., 2010). The average $RONO_2$ mixing ratios at TMS were much higher than those measured in forest areas in coastal New England (Russo et al., 2010) and in tropospheric air influenced by Asian outflow during the airborne TRACE-P mission (Simpson et al., 2003), where the levels of parent hydrocarbons were lower. (Note that all of the UCI data shown in Fig. 2 were adjusted to UCI's post-2008 $RONO_2$ calibration scale to enable direct comparison (Simpson et al., 2011)). However, the mean C_1–C_3 $RONO_2$ mixing ratios were slightly lower and the 2-$BuONO_2$ mixing ratio was higher at TMS than at Tai O (Table 2) and in Karachi, Pakistan (Barletta et al., 2002; the

ACPD
15, 22597–22636, 2015

Karachi data have also been adjusted to the new UCI $RONO_2$ calibration scale). The difference between TMS and Tai O might result from not only the levels of their parent hydrocarbons, but also the influence of air masses with different photochemical age and sources (see Sect. 3.2 for details). At the urban TW site, the mean $RONO_2$ mixing ratios were lower than those measured in urban areas in Europe (Worton et al., 2010) and China (Wang et al., 2013). Compared to the average values of $RONO_2$ at Tai O, the levels of $EtONO_2$, 1-$PrONO_2$ and 2-$BuONO_2$ were slightly higher and the $MeONO_2$ and 2-$PrONO_2$ mixing ratio was lower at TW. Nevertheless, the variations of $RONO_2$ in a specific region were influenced by sampling conditions, meteorological parameters, geophysical features, direct emissions and secondary formation distributions, and sources and variations of parent hydrocarbons.

3.1.2 Temporal variations

Day-to-day variations

Table 3 summarizes the synoptic weather conditions and the corresponding variations of O_3 and $RONO_2$ on all sampling days, i.e., the 10 O_3 episode days and 10 non-O_3 episode days. In general, weather conditions including temperatures, winds and solar radiation significantly influenced the levels of air pollutants. High O_3 and $RONO_2$ mixing ratios were generally associated with stable weather conditions, i.e., high temperatures, intense solar radiation and low wind speeds. For instance, after tropical cyclone Megi, which lasted from 12–24 October 2010, the weather turned fine and the mixing ratios of air pollutants, i.e., O_3 and $RONO_2$, clearly increased on 23 and 24 October 2010, accompanied by high temperatures (max: 23 and 31 °C at TMS and TW, respectively) and intense solar radiation levels (max: 843 and 851 $W\,m^{-2}$ for TMS and TW, respectively) on the two days. Furthermore, the mixing ratios of O_3 and $RONO_2$ increased significantly when there were continental anticyclones over mainland China, i.e., on 29 October–3 November, 9 and 19 November 2010, when temperatures and solar radiation levels increased and the northerly monsoon was enhanced. However, as the

ACPD
15, 22597–22636, 2015

weather changed, the mixing ratios of air pollutants changed correspondingly. For example, O_3 and $RONO_2$ levels were low on some non-O_3 episode days, i.e., 28 September, 2, 8 and 14 October 2010, when the weather conditions were unstable and rainfall was frequently observed before the sampling days (i.e., on 20–25 September, and 7 and 9–12 October 2010). Moreover, when the temperatures and solar radiation levels decreased and the prevailing winds were from the south and east, low levels of $RONO_2$ and O_3 were observed at both sites, i.e., on 27–28 October and 20–21 November 2010.

Figure 3 shows the time series of C_1–C_4 $RONO_2$ on O_3 episode and non-O_3 episode days at both sites. Although the ranges of $RONO_2$ mixing ratios were similar and peak values were found in the afternoon, the day-to-day variations of individual $RONO_2$ differed during the sampling period at both sites. The peak values were comparable and the diurnal patterns tracked each other well for C_2–C_4 $RONO_2$ at TMS and TW, especially on the days with relatively higher O_3 mixing ratios ($p < 0.05$), i.e., 24–31 October to 1–3 and 9 November, indicating the influence of photochemical production on the C_3–C_4 $RONO_2$ levels at both sites. The average daytime O_3 mixing ratios (07:00–18:00 LT) on the high O_3 days were 77 ± 3 and 38 ± 3 ppbv at TMS and TW, respectively, compared to 58 ± 3 and 23 ± 3 ppbv, respectively, on the non-O_3 episode days. The average daytime levels of 2-$PrONO_2$, 1-$PrONO_2$ and 2-$BuONO_2$ on high-level O_3 days at TMS were 27 ± 1 (TW: 28 ± 1), 4.5 ± 0.3 (4.4 ± 0.2) and 37 ± 2 (39 ± 3) pptv, respectively, higher than those on non-O_3 episode days ($p < 0.05$). For the C_1–C_2 $RONO_2$, the patterns of peaks and troughs of $MeONO_2$ and $EtONO_2$ were different at the two sites, especially on high-level O_3 days. The maximum $MeONO_2$ and $EtONO_2$ levels were found at midnight at TW and in the afternoon at TMS on some sampling days, i.e., 2 and 8 October, and 19–20 November. Overall, the differences in the day-to-day variations of $RONO_2$ resulted from differences in the contributions of direct emissions and secondary formation, levels of parent hydrocarbons, meteorological conditions and transport patterns (Guo et al., 2013a, b). The similarities in the day-to-day variations of $RONO_2$ probably resulted from similarities in the photochemical production and co-located parent hydrocarbon sources at both sites, apart from some interplay of air

ACPD
15, 22597–22636, 2015

masses between the two sites, which were further confirmed by the moderate to good correlations of C_2–C_4 $RONO_2$ at both sites (R^2 = 0.52–0.80). Indeed, previous studies found that mesoscale circulations, i.e., mountain-valley breeze, and regional transport had a significant influence on the redistribution of air pollutants between the two sites (Guo et al., 2013a; Ling et al., 2014).

Diurnal variations

Figure 4 presents the diurnal patterns of $RONO_2$ at the two sites. In general, the diurnal variations of C_2–C_4 $RONO_2$ on O_3 episode days were larger and the mixing ratios were higher than those on non-O_3 episode days at both sites ($p < 0.05$), confirming that secondary production of $RONO_2$ was more significant on O_3 episode days. In terms of $MeONO_2$, the levels were comparable ($p > 0.05$) and the diurnal patterns were similar between O_3 and non-O_3 episode days at both sites, probably due to the low production rate and long lifetime of $MeONO_2$. However, the diurnal patterns of C_2–C_4 $RONO_2$ varied across the two sites. At TMS, the hourly average mixing ratios of C_2–C_4 $RONO_2$ were lowest at ~ 07:00 LT, followed by a daytime buildup with the highest value in the afternoon, and a slow decrease until midnight. However, the maximum $RONO_2$ on O_3 episode days at TMS showed a delay, compared to that on non-O_3 episode days, implying that other factors, i.e., different transport patterns and photochemical production, might have more significant influence on the distributions of $RONO_2$ at TMS (Guo et al., 2013a). At TW, the diurnal features of $RONO_2$ on non-O_3 episode days were flatter than on O_3 episode days and the peaks were not statistically different from the troughs during daytime hours on non-O_3 episode days. In addition, relatively higher levels of $MeONO_2$ and $EtONO_2$ were observed from midnight to early morning, which could be associated with marine air masses originating from the South China Sea as the southerly winds prevailed (Guo et al., 2013a).

It is of interest to compare the diurnal patterns of $RONO_2$ in this study with the long-term observations at Tai O (n = 187), where 1 min samples were collected every 2 h from 07:00 to 19:00 LT on 15 selected pollution episode days from August 2001

ACPD
15, 22597–22636, 2015

to December 2002, with the remainder of samples collected every few days, typically in the mid-afternoon (Simpson et al., 2006). The highest pollution levels occurred on 7 November 2002, a similar season to this study. Although the diurnal variations of $RONO_2$ at Tai O during pollution episodes were similar to those observed in this study, i.e., minimum values in the early morning and a broad peak in the afternoon, some differences were found. The increment of $RONO_2$ during daytime hours was larger at Tai O. The average mixing ratios of $MeONO_2$, $EtONO_2$, 2-$PrONO_2$, 1-$PrONO_2$ and 2-$BuONO_2$ increased 17, 13, 27, 4.2 and 30 pptv from early morning to the afternoon at Tai O, respectively, about 1.5–3.8 times the increased values observed in this study. Furthermore, the diurnal patterns of C_1–C_4 $RONO_2$ at Tai O showed consistent troughs and peaks at 07:00 and 13:00 LT, whereas the minimum and maximum values of different $RONO_2$ appeared at different times at TMS and TW. This suggests that different $RONO_2$ shared common sources at Tai O, i.e., photochemical formation, while the source origins of $RONO_2$ in this study were more complicated.

3.2 Relationships of $RONO_2$ with parent hydrocarbons

3.2.1 Pure photochemical (PP) and background initial ratio (BIR) curves for the evolution of $RONO_2$

To investigate the photochemical evolution of $RONO_2$ at the two sites, the relationships of the $RONO_2$ with their parent hydrocarbons were further examined using a simplified sequential reaction model developed by Bertman et al. (1995) (Eq. 1), based on the assumptions that: (i) the hydrogen abstraction reaction from the parent hydrocarbon was the rate-limiting step for photochemical $RONO_2$ production; (ii) the reaction environment was NO_x-rich, making the reaction with NO the dominant pathway for the desctruction of RO_2 radicals; and (iii) the influence of the mixing processes was similar for $RONO_2$ and their parent hydrocarbons.

$$\frac{RONO_2}{RH} = \frac{\beta k_A}{k_B - k_A}\left(1 - e^{(k_A - k_B)t}\right) + \frac{[RONO_2]_0}{[RH]_0} e^{(k_A - k_B)t} \quad (1)$$

ACPD
15, 22597–22636, 2015

where $\beta = \alpha_1\alpha_2$, k_A is the production rate for the formation of $RONO_2$ through the oxidation of hydrocarbons, RH ($k_A = k_1[OH]$), while k_B is the destruction rate for $RONO_2$ through photolysis and the reaction with OH ($k_B = k_5[OH] + J_{RONO_2}$). $[RONO_2]_0$ and $[RH]_0$ are the initial concentrations of $RONO_2$ and the parent hydrocarbons before photochemical processing, respectively. [OH] is the diurnal average concentration of the OH radical. The relationships of $RONO_2$ with their parent hydrocarbons derived from the preceding equation are comparatively independent of the variations of OH and $RONO_2$ photolysis rates (Roberts et al., 1998; Wang et al., 2013). If the initial concentrations of $RONO_2$ and RH are zero, then Eq. (1) can be expressed as follows (Eq. 2):

$$\frac{RONO_2}{RH} = \frac{\beta k_A}{k_B - k_A}\left(1 - e^{(k_A - k_B)t}\right) \quad (2)$$

The relationships between $RONO_2$ and RH can be obtained by plotting the measured ratios of $RONO_2$/RH to a specific ratio, i.e., 2-$BuONO_2$/*n*-butane. 2-$BuONO_2$/*n*-butane was selected in this study because *n*-butane was one of the most abundant hydrocarbons and 2-$BuONO_2$ was the most dominant alkyl nitrate (Roberts et al., 1998; Wang et al., 2013; Worton et al., 2010). Although some studies have investigated the relationships between $RONO_2$ and their parent hydrocarbons using zero initial values of $RONO_2$, more recent studies have used non-zero initial values of $RONO_2$ to evaluate the influence of background levels on the photochemical evolution of $RONO_2$ (Reeves et al., 2007; Russo et al., 2010; Wang et al., 2013). Therefore, in addition to zero initial ratios, non-zero initial ratios of $RONO_2$/RH, equal to the lowest values from 00:00 to 07:00 LT measured at TMS and TW, respectively, were used to investigate the relationships between $RONO_2$ and their parent hydrocarbons in this study. The diurnal average OH mixing ratios were obtained from our previous study (Guo et al., 2013a). The curves drawn with zero initial values were the pure photochemical (PP) curves for the evolution of $RONO_2$, and the curves with non-zero values, defined as background initial ratio (BIR) curves, were drawn by assuming that both photochemical formation and

ACPD
15, 22597–22636, 2015

background levels contributed to the distribution of $RONO_2$ (Russo et al., 2010; Wang et al., 2013). Consistent with previous studies (Russo et al., 2010; Wang et al., 2013), the shapes of the BIR curves were different from those of PP curves. The BIR curves of C_1–C_3 $RONO_2$ at both sites laid above their PP curves at shorter processing time ($t < 1$ d) and converged towards the PP curves at longer processing times ($t = 1.5$–2 d), due to the decreased influence of the parameter $[RONO_2]_0/[RH]_0 e^{(k_A - k_B)t}$ on the difference between the two curves as the photochemical age increased (Wang et al., 2013). This feature was more obvious for C_3 $RONO_2$ at TW due to the lower values of $[RONO_2]_0/[RH]_0$ resulting from the high mixing ratios of propane at that site (Ling et al., 2014).

3.2.2 Ratios of $RONO_2$ to parent hydrocarbons

Calculations inferred that the ratios of C_2–C_4 $RONO_2$/RH were relatively lower at TW than at TMS ($p < 0.05$, Table 1), probably due to more fresh anthropogenic emissions and higher mixing ratios of parent hydrocarbons, i.e., ethane, propane and *n*-butane at the urban site of TW. The sources of the parent hydrocarbons observed at TW included vehicular exhaust and liquefied petroleum gas (LPG) usage (Ling et al., 2014). In terms of $MeONO_2$, since the levels of methane were comparable at the two sites, higher mixing ratio of $MeONO_2$ at TW led to a higher ratio of $MeONO_2$/methane.

Furthermore, we compared the C_1–C_4 $RONO_2$/RH ratios in this study with those at Tai O (Simpson et al., 2006). The ratios of C_3–C_4 $RONO_2$/RH at Tai O were higher than those at TW ($p < 0.05$) but slightly lower than those at TMS ($p = 0.05$), as the parent hydrocarbon levels at Tai O were higher than those at TMS, but lower than those at TW ($p < 0.05$). This was further confirmed by the photochemical age estimated by comparing the observed ratios and PP and BIR curves (Fig. 5). In addition, the higher ratios at Tai O than at TW might be related to the increase in C_2–C_4 hydrocarbons over the past 10 years (Ling et al., 2014). In 2001, the average mixing ratios of propane and *n*-butane were 2706±484 and 3722±629 pptv at TW (mean ±95 % confidence interval), respectively (Guo et al., 2004), and 2050±310 and 1640±305 pptv at Tai O, respectively

ACPD
15, 22597–22636, 2015

(Simpson et al., 2006). However, according to the current study, they increased to 3551 ± 415 and 4486 ± 482 pptv, respectively, at TW in 2010, about 1.35–2.11 times the mean levels of prppane and *n*-butane at Tai O in the same season (from September to November) in 2001–2002. Although higher C_2–C_4 hydrocarbon levels might increase the formation of C_2–C_4 $RONO_2$, the mixing ratios of C_3–C_4 $RONO_2$ at TW were slightly higher, only 1.02–1.1 times those at Tai O, probably due to the integrated effects of formation rates of $RONO_2$, distribution of different $RONO_2$ sources and contribution of local emissions and regional transport. Furthermore, the less increment of C_3–C_4 $RONO_2$ at TW may be also related to the decrease of NO_x over the past 10 years, with the reduction of 15 % from 2001 to 2010 at TW (HKEPD, http://epic.epd.gov.hk/EPICDI/air/station/). With regard to C_1–C_2 $RONO_2$, the ratio of $MeONO_2$/methane observed at Tai O was higher than that at TMS and TW ($p < 0.05$). The $MeONO_2$ level at Tai O was about 1.3–1.5 times the level observed in this study, and the methane mixing ratio was similar to that at TMS and TW. The variations of ethane and $EtONO_2$ at the three sites (Table 1 and Table 2) similarly resulted in higher ratios of $EtONO_2$/ethane at Tai O than those observed in this study ($p < 0.05$).

Overall, the abundance, distributions and ratios of C_1–C_4 $RONO_2$ and their parent hydrocarbons at TMS were different from those at TW, reflecting the different contributions of direct emissions and secondary formation of $RONO_2$ at the two sites.

3.2.3 Photochemical age of air masses

Figure 5 presents the relationship between C_1–C_3 $RONO_2$/RH and 2-$BuONO_2$/*n*-butane based on the measured values of C_1–C_4 $RONO_2$ and RH at TMS and TW. The photochemical age shown by the PP curves for the whole sampling period ranged from 6 h to 2 days at TMS, compared to < 30 min to 18 h at TW. However, when BIR curves were used, the photochemical age of air masses at TMS became 30 min to 1.5 days, yet it remained the same at TW. The similar photochemical age shown by both the PP and BIR curves at TW implies that the increment of $RONO_2$ during daytime hours was mainly due to the oxidation of locally emitted precursors (Cheung et al., 2014).

ACPD
15, 22597–22636, 2015

In comparison, the photochemical age of air masses at Tai O ranged from < 30 min to ~ 1.5 days (Fig. 5). This was consistent with the photochemical age of air masses at TMS, suggesting that the air masses arriving at the two sites were complex. Previous studies reported that the air masses arriving at Tai O originated from Hong Kong urban areas, the inland PRD region and the South China Sea (Wang et al., 2005; Simpson et al., 2006), while the air masses at TMS mainly orignated from the inland PRD region and the Hong Kong urban areas at the foot of the mountain (Guo et al., 2009). Furthermore, most of the observed ratios of C_1–C_4 $RONO_2$ to 2-$BuONO_2$/*n*-butane at TMS overlapped for O_3 and non-O_3 episode days, implying that the photochemical age of air masses at TMS was similar on both O_3 and non-O_3 episode days. This was consistent with the uniqueness of the sampling location, where air pollutants could be brought to TMS by mesoscale circulation and regional transport (Guo et al., 2013a). In contrast, the photochemical age of air masses was longer on O_3 episode days than on non-O_3 episode days at TW, with a range of 30 min to 18 h and < 30 min to 6 h on O_3 and non-O_3 episode days, respectively.

3.2.4 Comparison between the measured ratios of C_1–C_3 $RONO_2$/RH to 2-$BuONO_2$/*n*-butane and the pure photochemical curves

In addition to the ratios of $RONO_2$/RH and the photochemical age of air masses, a comparison of the measured ratios of C_1–C_3 $RONO_2$/RH to 2-$BuONO_2$/*n*-butane and PP and BIR curves could provide useful information about the evolution of $RONO_2$ at the two sites (Fig. 6).

At TMS, the measured ratios of $MeONO_2$/methane and $EtONO_2$/ethane to 2-$BuONO_2$/*n*-butane were much higher than the ratios in the PP curves (Fig. 6), with the trends approaching the PP curves at a longer processing time of 1.5–2 days. This suggested that the measured ratios of $MeONO_2$/methane and $EtONO_2$/ethane to 2-$BuONO_2$/*n*-butane were influenced by aged air masses due to the long atmospheric lifetimes and slow photochemical degradation rates of methane and ethane (Worton et al., 2010; Russo et al., 2010). However, the difference between the measured ratios

ACPD
15, 22597–22636, 2015

and the predicted ratios of C_1–C_2 $RONO_2$/RH to 2-$BuONO_2$/*n*-butane in BIR curves was comparatively smaller, further confirming the influence of background levels of C_1–C_2 $RONO_2$ and their parent hydrocarbons (i.e., the direct measurements of RH in Table 1) on the C_1–C_2 $RONO_2$/RH ratios (Wang et al., 2013), including both primary RH emissions and the formation of methyl and ethyl peroxy radicals from the decompostion of larger alkoxy radicals (Sommariva et al., 2008; Worton et al., 2010). Indeed, our previous field measurements found that the average mixing ratios of $MeONO_2$ and $EtONO_2$ at Hok Tsui, the PRD regional background site, were 4.9±0.3 and 5.3±0.4 pptv (non-published data), respectively, confirming the existence of background levels of ambient $RONO_2$.

With regard to C_3 $RONO_2$, the measured ratios of 1- and 2-$PrONO_2$/propane to 2-$BuONO_2$/*n*-butane were closer to the ratios of the BIR curve than those of the PP curve at TMS, further revealing the influence of background C_3 $RONO_2$ and their parent hydrocarbons at that site. However, the evolution of the measured ratios of C_2 $RONO_2$/RH to 2-$BuON_2$/*n*-butane agreed well with the predicted ratios of BIR and PP curves at TMS, indicating that secondary formation from propane oxidation contributed significantly to the ambient C_2 $RONO_2$ levels, including the background C_3 $RONO_2$. Consistent with previous studies, the slopes for the observed ratios of C_2 $RONO_2$/RH to 2-$BuONO_2$/*n*-butane and those in the PP and BIR curves were different (Russo et al., 2010; Wang et al., 2013). For example, the slopes of the observed ratios of 1- and 2-$PrONO_2$/propane to 2-$BuONO_2$/*n*-butane were 0.04 ± 0.01 and 0.26 ± 0.02, respectively, and the slopes for the BIR curves were 0.02 ± 0.01 (PP curve: 0.02 ± 0.01) and 0.12 ± 0.01 (0.10 ± 0.01), respectively. This was reasonable due to the difference in the number of samples and distribution of data between the observed ratios and the ratios of PP and BIR curves, particularly when the observed ratios were higher than the theoretical ones due to the significant influence of background levels of $RONO_2$ and RH (Russo et al., 2010; Wang et al., 2013). Therefore, to further investigate the influence of secondary formation and backround mixing ratios on C_3 $RONO_2$ at TMS, the ratio of 1-/2-$PrONO_2$ was analyzed. Previous studies have reported that the theoretical ratio

ACPD
15, 22597–22636, 2015

of 1-/2-$PrONO_2$ was the ratio between the yield for 1-$PrONO_2$ and 2-$PrONO_2$ formation, which was equal to the ratio of $\beta_{1-PrONO_2}/\beta_{2-PrONO_2}$ (0.21) (Simpson et al., 2003; Wang et al., 2013). If photochemical production was the dominant source of 1-$PrONO_2$ and 2-$PrONO_2$, the observed ratios should be close to the theoretical ones. Indeed, the slope of 1-$PrONO_2$ and 2-$PrONO_2$ at TMS was 0.19 (R^2 = 0.86, $p < 0.05$), close to the theoretical ratio (0.21) (Simpson et al., 2003; Wang et al., 2013), confirming that photochemical production from propane, including photochemical in-situ production and transport of photochemically-formed C_3 $RONO_2$ in urban areas and/or during transit from urban areas to TMS, was the dominant source of ambient C_3 $RONO_2$.

At TW, the comparison between the observed ratios of C_1–C_2 $RONO_2$/RH to 2-$BuONO_2$/*n*-butane and the ratios from the PP and BIR curves was consistent with that at TMS. However, in terms of C_3 $RONO_2$, although the evolution of the measured ratios of C_3 $RONO_2$/RH to 2-$BuONO_2$/*n*-butane followed the trends of the ratios in the PP and BIR curves, the measured ratios of C_3 $RONO_2$/RH to 2-$BuONO_2$/*n*-butane at TW were further away from the PP/BIR curves, i.e., about 2–3 times the ratios in the PP and BIR curves, implying additional sources of C_3 $RONO_2$ (Wang et al., 2013) at that site. High emissions of propane provided sufficient precursors of C_3 $RONO_2$, and the lifetimes of propane, 1-$PrONO_2$ and 2-$PrONO_2$ were long enough to sustain relatively high levels at TW. To further investigate the influence of additional sources on the distributions of C_3 $RONO_2$ at TW, Eq. (1) was used to fit the measured ratios of 1- and 2-$PrONO_2$/propane to calculate the yield of C_2 $RONO_2$ (β) (Wang et al., 2013). The average yields of 1- and 2-$PrONO_2$ were 0.032 ± 0.004 and 0.22 ± 0.02, respectively, higher than the laboratory kinetic values by factors of 4–9 (Kwok and Atkinson, 1995). This confirmed the existence of additional emissions of C_3 $RONO_2$ at TW, i.e., locally-emitted C_3 $RONO_2$ and/or secondary formation other than the production pathway from propane to proxyl radical and $PrONO_2$ (Reeves et al., 2007; Worton et al., 2010). Indeed, the slope of 1-$PrONO_2$ to 2-$PrONO_2$ at TW was 0.15 (R^2 = 0.80, $p < 0.05$), lower than the theoretical ratio of 1-$PrONO_2$/2-$PrONO_2$, further demonstrating the influence of other significant sources on ambient C_3 $RONO_2$ mixing ratios at TW.

ACPD
15, 22597–22636, 2015

In comparison, the observed ratios of C_1–C_3 $RONO_2$/RH to 2-$BuONO_2$/*n*-butane were higher than the PP curves at Tai O, indicating the contributions of background levels to ambient $RONO_2$ at that site as well. However, in addition to C_3 $RONO_2$, the tendencies of the observed ratios of C_1–C_2 $RONO_2$/RH to 2-$BuONO_2$/*n*-butane showed the same patterns as the BIR curves at Tai O, which were different from those at TMS and TW, suggesting that photochemical oxidation had a significant influence on the variations of $RONO_2$ at Tai O (Simpson et al., 2006). Furthermore, most of the observed ratios of $MeONO_2$/methane to 2-$BuONO_2$/*n*-butane at Tai O were scattered between the PP and BIR curves, especially at long photochemical processing times (12 h to 1.5 days), reflecting the potential influence from other sink mechanisms of $MeONO_2$ at long processing times at that site (Russo et al., 2010; Wu et al., 2011; Lyu et al., 2015). Consistent with those at TW, the measured ratios of C_3 $RONO_2$/RH to 2-$BuONO_2$/*n*-butane were above the BIR curves at Tai O, also suggesting the existence of additional sources of C_3 $RONO_2$ (Lyu et al., 2015).

3.3 Source apportionment of $RONO_2$

Figure 6 presents the explained variations of species (as a percentage of the species total) in the identified sources extracted by the PMF model. The standard errors in the figure were obtained from a bootstrap analysis of the PMF model simulation.

High O_x and $RONO_2$ concentrations were found in the first factor at both sites, implying that this factor was associated with secondary formation. In addition, certain amounts of combustion species, i.e., ethane, ethyne, propane, *n*/*i*-butanes, benzene and CO were present in this factor. It is not surprising that O_x correlated with the aforementioned species given that O_3 is a secondary pollutant formed from the photochemical oxidation of RH (Ling and Guo, 2014). The second factor was distinguished by a significant presence of methyl chloride, ethene, ethyne and benzene along with certain amounts of methane, propane and *n*/*i*-butane. It is well established that methyl chloride, ethyne and benzene are typical tracers for biomass burning/biofuel combustion (Barletta et al., 2009; Guo et al., 2011). As biofuel was not in widespread use in

ACPD
15, 22597–22636, 2015

Hong Kong (HKCSD, 2010), this factor was identified as biomass burning. The third factor was identified as oceanic emissions, as the tracer DMS had an exclusively high percentage in this source at both sites (Blake et al., 2003; Marandino et al., 2013). The last factor was dominated by high percentages of propane and *n*/*i*-butanes, typical tracers of LPG. Therefore, this factor was identified as LPG usage.

By summing up the mass of the $RONO_2$ in each source, the total concentrations of $RONO_2$ in each source were obtained and the contribution of each individual source to $RONO_2$ at both sites was calculated. Secondary formation was the most significant contributor to ambient $RONO_2$ at TMS and TW, on average about 65 ± 2 % and 54 ± 1 %, respectively, in line with the results in Sects. 3.2.2 and 3.2.3. The second largest contributor was biomass burning, with average percentages of 29 ± 1 % and 40 ± 2 % at TMS and TW, respectively, and oceanic emissions contributed the rest. The identification and contributions of biomass burning and oceanic emissions suggested that they caused the discrepancies between the predicted and observed ratios at the two sites (see Sect. 3.2.3). The significant contributions of biomass burning at the two sites might be attributable to biomass burning activities in the small villages nearby in addition to the frequent barbecue activities at the foot of the mountain, consistent with the findings in our previous study (Guo et al., 2013a, b). Moreover, the additional contributions of biomass burning at TMS could be related to air masses from the PRD region (Guo et al., 2012, 2013a). Indeed, although the patterns of surface winds were different at the two sites, our previous studies demonstrated that the air pollutants at TMS were influenced by the urban areas at the foot of the mountain (Hong Kong and the inland PRD region) due to the combined effect of mesocale circulation and regional transport (Guo et al., 2012, 2013a, b).

In contrast to the source apportionments at TMS and TW, the contributions of secondary formation and biomass burning to the ambient $RONO_2$ at Tai O were statistically equal, with average values of 46 ± 2 and 49 ± 3 %, respectively (Wang et al., 2005).

ACPD
15, 22597–22636, 2015

4 Conclusions

Intensive field measurements of $RONO_2$ and their parent hydrocarbons were conducted concurrently at a mountain site (TMS) and an urban site (TW) at the foot of the same mountain in Hong Kong from September to November 2010. C_1–C_4 $RONO_2$ presented different levels and temporal patterns at the two sites, indicating different contributions of primary and secondary sources of $RONO_2$ at the two sites. The ratios of C_2–C_4 $RONO_2$/RH were lower at TW than at TMS due to a greater amount of fresh anthropogenic emissions and higher mixing ratios of hydrocarbons at TW. The higher mixing ratio of $MeONO_2$/methane at TW was related to the higher level of $MeONO_2$ at TW and comparable levels of methane at the two sites. The photochemical age of the sampled air masses was similar on both O_3 and non-O_3 episode days at TMS due to the significant influence of mesoscale circulations and regional transport at that site. In contrast, the air masses were more aged on O_3 episode days at TW. Furthermore, the difference between the measured ratios of C_1–C_3 $RONO_2$/RH to 2-$BuONO_2$/*n*-butane and the background initial ratio curves, together with the direct measurements of RH and $RONO_2$, confirmed the existence of background levels of $RONO_2$ and RH at both sites. At TMS, the good agreement between the evolution of the measured ratios of C_3 $RONO_2$/RH to 2-$BuON_2$/*n*-butane and the ratios of BIR and PP curves suggested that C_3 $RONO_2$ were related to secondary formation from propane oxidation. This was further confirmed by the ratios of 1-/2-$PrONO_2$. The ratios of 1-/2-$PrONO_2$ and yield of $PrONO_2$ at TW revealed that in addition to the photochemical oxidation of propane, other sources including locally emitted and other secondary pathways had significant influences on C_3 $RONO_2$ mixing ratios at that site. The source apportionment results suggested that secondary formation contributed to the majority of the $RONO_2$ at TMS, whereas secondary formation and biomass burning were the major contributors to ambient $RONO_2$, followed by oceanic emissions at TW. Overall, the evolution of $RONO_2$ and its influencing factors in subtropical Hong Kong are consistent with those in other environments. Given the dominant contributions of secondary formation, background

ACPD
15, 22597–22636, 2015

levels of $RONO_2$ and their parent hydrocarbons have significant influences on the distributions of $RONO_2$ in Hong Kong.

The Supplement related to this article is available online at doi:10.5194/acpd-15-22597-2015-supplement.

Acknowledgements. This project was supported by the Research Grants Council of the Hong Kong Special Administrative Region via grants PolyU5179/09E, PolyU5154/13E and PolyU152052/14E. This study was partly supported by the internal grants of the Hong Kong Polytechnic University (87UB and 1-ZVCX), the Public Policy Research Funding Scheme (2013.A6.012.13A) and the National Natural Science Foundation of China (No. 41405112 and 41275122).

References

AFCD (Agriculture, Fisheries and Conservation Department): Country Parks and Special Areas Distribution Map–Tai Mo Shan Park, available at: http://www.afcd.gov.hk/english/country/cou_vis/cou_vis_cou/cou_vis_cou.html, last access: 18 August 2015.

Archibald, A. T., Khan, M. A. H., Watson, L. A., Utembe, S. R., Shallcross, D. E., Clemitshaw, K. C., and Jenkin, M. E.: Comment on 'Long-term atmospheric measurements of C_1–C_5 alkyl nitrates in the Pearl River Delta region of southeast China' by Simpson et al., Atmos. Environ., 41, 7369–7370, 2007.

Arey, J., Aschmann, S. M., Kwok, E. S. C., and Atkinson, R.: Alkyl nitrate, hydroxyl nitrate, and hydroxycarbonyl formation from the NO_x-air photooxidations of C_5–C_8 *n*-alkanes. J. Phys. Chem.-US, 105, 1020–1027, 2001.

Atkinson, R., Aschmann, S. M., Carter, W. P. L., Winer, A. M., and Pitts Jr., J. N.: Alkyl nitrate formation from the NO_x-air photooxidations of C_2–C_8 *n*-alkanes, J. Phys. Chem.-US, 86, 4563–4569, 1982.

Atkinson, R., Baulch, D. L., Cox, R. A., Crowley, J. N., Hampson, R. F., Hynes, R. G., Jenkin, M. E., Rossi, M. J., Troe, J., and IUPAC Subcommittee: Evaluated kinetic and photochemical

ACPD
15, 22597–22636, 2015

data for atmospheric chemistry: Volume II gas phase reactions of organic species, Atmos. Chem. Phys., 6, 3625–4055, doi:10.5194/acp-6-3625-2006, 2006.
Atlas, E.: Evidence for ≥ C_2 alkyl nitrates in rural and remote atmospheres, Nature, 4, 426–428, 1998.
Barletta, B., Meinardi, S., Simpson, I. J., Khwaja, H. A., Blake, D. R., and Rowland, F. S.: Mixing ratios of volatile organic compounds (VOCs) in the atmosphere of Karachi, Pakistan, Atmos. Environ., 36, 3429–3443, 2002.
Barletta, B., Meinardi, S., Simpson, I. J., Atlas, E. L., Beyersdorf, A. J., Baker, A. K., Blake, N. J., Yang, M., Midyett, J. R., Novak, B. J., McKeachie, R. J., Fuelberg, H. E., Sachse, G. W., Avery, M. A., Campos, T., Weinheimer, A. J., Rowland, F. S., and Blake, D. R.: Characterization of volatile organic compounds (VOCs) in Asian and north American pollution plumes during INTEX-B: identification of specific Chinese air mass tracers, Atmos. Chem. Phys., 9, 5371–5388, doi:10.5194/acp-9-5371-2009, 2009.
Bertman, S. B., Roberts, J. M., Parrish, D. D., Buhr, M. P., Goldan, P. D., Kuster, W. C., Fehsenfeld, F. C., Montzka, S. A., and Westberg, H.: Evolution of alkyl nitrates with air mass age, J. Geophys. Res., 100, 22805–22813, 1995.
Blake, N. J., Blake, D. R., Swanson, A. L., Atlas, E., Flocke, F., and Rowland, F. S.: Latitudinal, vertical, and seasonal variations of C_1–C_4 alkyl nitrates in the troposphere over the Pacific Ocean during PEM-Tropics A and B: Oceanic and continental sources, J. Geophys. Res., 108, 8242, doi:10.1029/2001JD001444, 2003.
Cheung, K., Guo, H., Ou, J. M., Simpson, I. J., Barletta, B., Meinardi, S., and Blake, D. R.: Diurnal profiles of isoprene, methacrolein and methyl vinyl ketone at an urban site in Hong Kong, Atmos. Environ., 84, 323–331, 2014.
Clemitshaw, K. C., Williams, J., Rattigan, O. V., Shallcross, D. E., Law, K. S., and Cox, R. A.: Gas-phase ultraviolet absorption cross-sections and atmospheric lifetimes of several C_2–C_5 alkyl nitrates, J. Photoch. Photobio. A, 102, 117–126, 1997.
Colman, J. J., Swanson, A. L., Meinardi, S., Sive, B. C., Blake, D. R., and Rowland, F. S.: Description of the analysis of a wide range of volatile organic compounds in whole air samples collected during PEM-Tropics A and B, Anal. Chem., 73, 3723–3731, 2001.
Friend, A. J., Ayoko, G. A., Stelcer, E., and Cohen, D.: Source apportionment of $PM_{2.5}$ at two receptor sites in Brisbane, Australia, Environ. Chem., 8, 569–580, 2011.

ACPD
15, 22597–22636, 2015

Guo, H., Wang, T., and Louie, P. K. K.: Source apportionment of ambient non-methane hydrocarbons in Hong Kong: application of a principal component analysis/absolute principal component scores (PCA/APCS) receptor model, Environ. Pollut., 129, 489–498, 2004.

Guo, H., Jiang, F., Cheng, H. R., Simpson, I. J., Wang, X. M., Ding, A. J., Wang, T. J., Saunders, S. M., Wang, T., Lam, S. H. M., Blake, D. R., Zhang, Y. L., and Xie, M.: Concurrent observations of air pollutants at two sites in the Pearl River Delta and the implication of regional transport, Atmos. Chem. Phys., 9, 7343–7360, doi:10.5194/acp-9-7343-2009, 2009.

Guo, H., Ling, Z. H., Simpson, I. J., Blake, D. R., and Wang, D. W.: Observations of isoprene, methacrolein (MAC) and methyl vinyl ketone (MVK) at a mountain site in Hong Kong, J. Geophys. Res., 117, D19303, 1–13, doi:10.1029/2012JD017750, 2012.

Guo, H., Ling, Z. H., Cheung, K., Jiang, F., Wang, D. W., Simpson, I. J., Barletta, B., Meinardi, S., Wang, T. J., Wang, X. M., Saunders, S. M., and Blake, D. R.: Characterization of photochemical pollution at different elevations in mountainous areas in Hong Kong, Atmos. Chem. Phys., 13, 3881–3898, doi:10.5194/acp-13-3881-2013, 2013a.

Guo, H., Ling, Z. H., Cheung, K., Wang, D. W., Simpson, I. J., and Blake, D. R.: Acetone in the atmosphere of Hong Kong: Abundance, sources and photochemical precursors, Atmos. Environ., 65, 80–88, 2013b.

HKCSD (Hong Kong Census and Statistics Department): Hong Kong Annual Digest of Statistics 2010, http://www.statistics.gov.hk/pub/B10100032010AN10B0100.pdf (last access: 18 August 2015), 2010.

HKEPD (Hong Kong Environmental Protection Department): Air Quality in Hong Kong 2011, http://www.epd-asg.gov.hk/tc/download/air-quality-reports.html (last access: 18 August 2015), 2012.

Jenkin, M. E. and Clemitshaw, C.: Ozone and other secondary photochemical pollutants: Chemical processes governing their formation in the planetary boundary layer, Atmos. Environ., 34, 2499–2527, 2000.

Kwok, E. S. C. and Atkinson, R.: Estimation of hydroxyl radical reaction-rate constants for gas-phase organic-compounds using a structure-reactivity relationship-an update, Atmos. Environ., 29, 1685–1695, 1995.

Ling, Z. H. and Guo, H.: Contribution of VOC sources to photochemical ozone formation and its control policy implication in Hong Kong, Environ. Sci. Policy, 38, 180–191, 2014.

ACPD
15, 22597–22636, 2015

Ling, Z. H., Guo, H., Cheng, H. R., and Yu, Y. F.: Sources of ambient volatile organic compounds and their contributions to photochemical ozone formation at a site in the Pearl River Delta, southern China, Environ. Pollut., 159, 2310–2319, 2011.

Ling, Z. H., Guo, H., Zheng, J. Y., Louie, P. K. K., Cheng, H. R., Jiang, F., Cheung, K., Wong, L. C., and Feng, X. Q.: Establishing a conceptual model for photochemical ozone pollution in subtropical Hong Kong, Atmos. Environ., 76, 208–220, 2013.

Lyu, X. P., Ling, Z. H., Guo, H., Saunders, S. M., Lam, S. H. M., Wang, N., Wang, Y., Liu, M., and Wang, T.: Re-examination of C_1–C_5 alkyl nitrates in Hong Kong using an observation-based model, accepted, 2015.

Marandino, C. A., Tegtmeier, S., Krüger, K., Zindler, C., Atlas, E. L., Moore, F., and Bange, H. W.: Dimethylsulphide (DMS) emissions from the western Pacific Ocean: a potential marine source for stratospheric sulphur?, Atmos. Chem. Phys., 13, 8427–8437, doi:10.5194/acp-13-8427-2013, 2013.

Paatero, P.: User's guide for Positive Matrix Factorization Programs PMF2 and PMF3, Part 1: Tutorial, Prepared by University of Helsinki, Helsinki, 2000.

Reeves, C. E., Slemr, J., Oram, D. E., Worton, D., Penkett, S. A., Stewart, D. J., Purvis, R., Watson, N., Hopkins, J., Lewis, A., Methven, J., Blake, D. R., and Atlas, E.: Alkyl nitrates in outflow from North America over the North Atlantic during intercontinental transport of ozone and precursors 2004, J. Geophys. Res., 112, D10S037, doi:10.1029/2006JD007567, 2007.

Roberts, J. M.: The atmospheric chemistry of organic nitrates, Atmos. Environ., 24A, 243–287, 1990.

Roberts, J. M., Bertman, S. B., Parrish, D. D., Fehsenfeld, F. C., Johnson, B. T., and Niki, H.: Measurements of alkyl nitrates at Chebogue Point Nova Scotia during the 1993 North Atlantic Regional Experiment (NARE) intensive, J. Geophys. Res., 103, 13569–13580, 1998.

Rosen, R. S., Wood, E. C., Wooldridge, P. J., Thornton, J. A., Day, D. A., Kuster, W., Williams, E. J., Jobson, B. T., and Cohen, R. C.: Observations of total alkyl nitrates during Texas Air Quality Study 2000: implications for O_3 and alkyl nitrate photochemistry, J. Geophys. Res., 109, D07303, doi:10.1029/2003JD004227, 2004.

Russo, R. S., Zhou, Y., Haase, K. B., Wingenter, O. W., Frinak, E. K., Mao, H., Talbot, R. W., and Sive, B. C.: Temporal variability, sources, and sinks of C_1–C_5 alkyl nitrates in coastal New England, Atmos. Chem. Phys., 10, 1865–1883, doi:10.5194/acp-10-1865-2010, 2010.

Seinfeld, J. H. and Pandis, S. N.: Atmospheric Chemistry and Physics: From Air Pollution to Climate Change, 2nd edn, Wiley Publishers, New York, USA, 2006.

ACPD
15, 22597–22636, 2015

Simpson, I. J., Meinardi, S., Blake, D. R., and Blake, N. J.: A biomass burning source of C_1–C_4 alkyl nitrates, Geophys. Res. Lett., 29, 2168, doi:10.1029/2002GL016290, 2002.
Simpson, I. J., Blake, N. J., Blake, D. R., Atlas, E., Flocke, F., Crawford, J. H., Fuelberg, H. E., Kiley, C. M., Meinardi, S., and Rowland, F. S.: Photochemical production and evolution of selected C_2–C_5 alkyl nitrates in tropospheric air influenced by Asia outflow, J. Geophys. Res., 108, D20, doi:10.1029/2002JD002830, 2003.
Simpson, I. J., Wang, T., Guo, H., Kwok, Y. H., Flocke, F., Atlas, E., Meinardi, S., Rowland, F. S., and Blake, D. R.: Long-term atmospheric measurements of C_1–C_5 alkyl nitrates in the Pearl River Delta region of southeast China, Atmos. Environ., 40, 1619–1632, 2006.
Simpson, I. J., Blake, N. J., Barletta, B., Diskin, G. S., Fuelberg, H. E., Gorham, K., Huey, L. G., Meinardi, S., Rowland, F. S., Vay, S. A., Weinheimer, A. J., Yang, M., and Blake, D. R.: Characterization of trace gases measured over Alberta oil sands mining operations: 76 speciated C_2–C_{10} volatile organic compounds (VOCs), CO_2, CH_4, CO, NO, NO_2, NO_y, O_3 and SO_2, Atmos. Chem. Phys., 10, 11931–11954, doi:10.5194/acp-10-11931-2010, 2010.
Simpson, I. J., Akagi, S. K., Barletta, B., Blake, N. J., Choi, Y., Diskin, G. S., Fried, A., Fuelberg, H. E., Meinardi, S., Rowland, F. S., Vay, S. A., Weinheimer, A. J., Wennberg, P. O., Wiebring, P., Wisthaler, A., Yang, M., Yokelson, R. J., and Blake, D. R.: Boreal forest fire emissions in fresh Canadian smoke plumes: C_1–C_{10} volatile organic compounds (VOCs), CO_2, CO, NO_2, NO, HCN and CH_3CN, Atmos. Chem. Phys., 11, 6445–6463, doi:10.5194/acp-11-6445-2011, 2011.
Sommariva, R., Trainer, M., de Gouw, J. A., Roberts, J. M., Warneke, C., Atlas, E., Flocke, F., Goldan, P. D., Kuster, W. C., Swanson, A. L., and Fehsenfeld, F. C.: A study of organic nitrates formation in an urban plume using a Master Chemical Mechanism, Atmos. Environ., 42, 5771–5786, 2008.
Talukdar, R. K., Burkholder, J. B., Hunter, M., Gilles, M. K., Roberts, J. M., and Ravishankara, A. R.: Atmospheric fate of several alkyl nitrates Part 2 UV absorption cross-sections and photodissociation quantum yields, J. Chem. Soc. Faraday T., 93, 2797–2805, 1997.
Wang, M., Shao, M., Chen, W. T., Lu, S. H., Wang, C., Huang, D. K., Yuan, B., Zeng, L. M., and Zhao, Y.: Measurements of C_1–C_4 alkyl nitrates and their relationships with carbonyl compounds and O_3 in Chinese cities, Atmos. Environ., 81, 389–398, 2013.
Wang, T., Guo, H., Blake, D. R., Kwok, Y. H., Simpson, I. J., and Li, Y. S.: Measurements of trace gases in the inflow of South China Sea background air and outflow of regional pollution at Tai O, Southern China, J. Atmos. Chem., 52, 295–317, 2005.

ACPD
15, 22597–22636, 2015

Worton, D. R., Reeves, C. E., Penkett, S. A., Sturges, W. T., Slemr, J., Oram, D. E., Bandy, B. J., Bloss, W. J., Carslaw, N., Davey, J., Emmerson, K. M., Gravestock, T. J., Hamilton, J. F., Heard, D. E., Hopkins, J. R., Hulse, A., Ingram, T., Jacob, M. J., Lee, J. D., Leigh, R. J., Lewis, A. C., Monks, P. S., and Smith, S. C.: Alkyl nitrate photochemistry during the tropospheric organic chemistry experiment, Atmos. Environ., 44, 773–785, 2010.

Wu, Z. Y., Wang, X. M., Chen, F., Turnipseed, A. A., Guenther, A., Niyogi, D., Charusombat, U., Xia, B. C., Munger, J. W., and Alapty, K.: Evaluating the calculated dry deposition velocities of reactive nitrogen oxides and ozone from two community models over a temperate deciduousforest, Atmos. Environ., 45, 2633–2674, 2011.

ACPD
15, 22597–22636, 2015

Table 1. Statistical description of alkyl nitrate and parent hydrocarbon mixing ratios (pptv) for whole air samples collected at TMS and TW during the sampling period.

Species	TMS Mean[a]	Min	Max	TW Mean	Min	Max
$MeONO_2$	10.9 ± 0.4	6.2	21.4	12.6 ± 0.5	7.2	26.6
$EtONO_2$	12.1 ± 0.5	3.2	25.6	13.3 ± 0.6	4.0	35.0
2-$PrONO_2$	24.1 ± 1.1	4.0	51.2	26.3 ± 1.2	6.0	49.2
1-$PrONO_2$	3.8 ± 0.2	0.4	10.6	4.0 ± 0.2	0.7	8.1
2-$BuONO_2$	32.0 ± 1.7	3.1	80.1	34.2 ± 1.9	5.1	92.8
Methane (ppmv)	2.0 ± 0.1	1.8	2.2	2.0 ± 0.1	1.8	2.5
Ethane	1908 ± 78	396	3588	2224 ± 90	717	4315
Propane	1101 ± 75	106	4455	3551 ± 415	1443	33 800
n-Butane	830 ± 91	97	6252	4486 ± 482	1372	34 700

[a] Average ±95 % confidence interval

ACPD
15, 22597–22636, 2015

Table 2. Alkyl nitrate and parent hydrocarbon mixing ratio statistics (pptv) for whole air samples collected at Tai O between 24 August 2001 and 31 December 2002 from Simpson et al. (2006).

Compound	Minimum	Maximum	Median	Mean
$MeONO_2$	5.5	52.2	13.4	15.9
$EtONO_2$	2.7	34.3	12.1	13.1
1-$PrONO_2$	0.2	14.5	3.5	3.9
2-$PrONO_2$	2.4	65.9	24.5	32.6
2-$BuONO_2$	0.8	89.8	27.4	30.7
Methane	1 749 000	3 702 000	1 956 000	2 052 000
Ethane	375	5050	2135	2120
Propane	6	12 995	1545	2050
n-Butane	6	12 790	950	1640

ACPD
15, 22597–22636, 2015

Table 3. Summary of synoptic weather conditions and the corresponding variations of air pollutants on the sampling O_3 and non-O_3 episode days.

Sampling days	Synoptic weather conditions	Variation of pollutants
O_3 episode day		
23–24 Oct 2010	After the tropical cyclone Megi, the weather turned fine. The temperature (max: 23 and 31 °C at TMS and TW, respectively) and solar radiation levels (max: 843 and 851 W m^{-2}, respectively) increased and remained at high levels. The wind speed decreased and the prevailing wind direction was from the north at TMS. The prevailing winds at TW changed from southeast on 23 October to north on 24 October.	O_3, NO and SO_2 increased clearly and CO increased moderately. O_3 reached peaks of 137 ppbv at TMS and 85 ppbv at TW. SO_2 reached 10 ppbv at TMS and 14 ppbv at TW. The mixing ratios of $RONO_2$ increased clearly and the diurnal patterns of alkyl nitrates were more significant with peak values observed in the afternoon. The diurnal patterns tracked each other well for C_2–C_4 $RONO_2$ at TMS and TW.
29 Oct–03 Nov 2010	With a continental anticyclone over mainland China, the temperature started to increase and the weather was fine. A northerly dry monsoon was enhanced at both sites. The solar radiation levels were higher at TMS than that at TW, where their peaks reached 811 and 800 W m^{-2}, respectively. The winds were mostly from the north at TMS, and those at TW were from the southeast, east and northeast.	O_3 increased and stayed at high levels at TMS. SO_2 and CO at the two sites exhibited an increasing trend and a broad peak. The levels of $RONO_2$ were slightly lower than those on 23 and 24 October at both sites. The diurnal patterns of C_1–C_2 $RONO_2$ with troughs and peaks during daytime hours were observed on 29 October– 3 November at both sites.
09 Nov 2010	A continental anticyclone controlled northwestern China. After rainy days on 4–6 November, the weather turned fine and stable. The temperatures and solar radiation levels increased and the wind speeds decreased.	O_3 stayed at a level above 100 ppbv at TMS. NO remained stable and the levels CO and SO_2 fluctuated. The levels of $RONO_2$ increased significantly at TMS and TW, with peaks observed in the afternoon.

ACPD
15, 22597–22636, 2015

Table 3. Continued.

Sampling days	Synoptic weather conditions	Variation of pollutants
19 Nov 2010	The anticyclone moved over northeastern China and the East China Sea. Although the prevailing direction was from the north at both sites, the wind speeds decreased. The solar radiation levels were higher at TMS than those at TW, with maximum values of 673 and 555 W m^{-2}, respectively.	O_3 increased sharply and reached peaks higher than 110 ppb at TMS. CO had a broad peak at both sites. The peak values of $RONO_2$ increased significantly. C_3 and C_4 $RONO_2$ peaked in the afternoon at the two sites. The maximum $MeONO_2$ and $EtONO_2$ levels were observed at midnight at TW and in the afternoon at TMS on some sampling days.
Non-O_3 episode days		
28 Sep, 02, 08 and 14 Oct 2010	Low-pressure systems were located in the PRD region and Hainan province on 28 September and 8 October. The weather turned to cloudy in the afternoon on these two days. On 2 and 14 October, low-pressure systems (trough) were observed in northern and southern China. The temperatures and solar radiation levels were high on these two days, reaching daily maximum values of 24–27 °C and 775–886 W m^{-2}, respectively. The winds were mostly from the southeast at TW, those at TMS were from the east and northeast at low speeds. Rainfall was observed on the days of 20–25 September, 7, and 9–12 October.	The levels of O_3 and $RONO_2$ were low at TMS and TW on 28 September and 2 October. Over the 4 sampling days, the maximum levels of O_3 and $RONO_2$ were observed on 8 October, with O_3 (total $RONO_2$) reaching peaks of 97 ppbv (125 pptv) at TMS and 65 ppbv (129 pptv) at TW.

ACPD
15, 22597–22636, 2015

Table 3. Continued.

Sampling days	Synoptic weather conditions	Variation of pollutants
18–19 Oct 2010	The tropical cyclones Megi was formed in the South China Sea. The temperature and solar radiation started to decrease from 18 to 19 Oct. The prevailing winds were from the north at TMS and changed from southeast to north from 18 to 19 October at TW.	The daily maximum levels of O_3 decreased from 95 ppbv on 18 October to 85 ppbv on 19 October at TMS. Diurnal patterns with maximum values in the afternoon were observed for $RONO_2$ at TMS and TW.
27–28 Oct 2010	The tropical cyclone S.T.Chaba was located about 600 km east of Taiwan in the Philippine Sea and moving north. The winds at the two sites were mostly from the north. The temperature started to decrease, with daily maximum values reaching 16 and 25 °C at TMS and TW, respectively.	Air pollutants started to accumulate. The maximum levels of O_3 reached 80 and 50 ppbv at TMS and TW, respectively. The levels of $RONO_2$ on these two days were lower than those on 23 and 24 October, reaching maximum total levels of of 95 and 94 pptv at TMS and TW, respectively.
20–21 Nov 2010	On the south edge of the high-pressure system located in North China, the weather was fine. Prevailing southeast winds were observed at TW. The prevailing winds at TMS were from the east. The solar radiation levels were low on 20 November, reaching maximum values of 428 and 507 $W m^{-2}$ at TMS and TW, respectively.	O_3 concentrations decreased to low levels at TMS and TW, with maximum hourly average values of 67 and 33 ppbv, respectively. The levels of $RONO_2$ decreased at the two sites on 19 Nov. High $RONO_2$ mixing ratios were observed at midnight at TW.

ACPD
15, 22597–22636, 2015

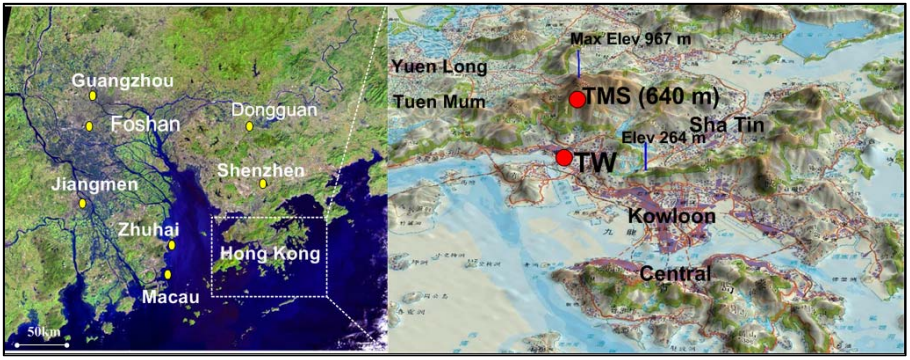

Figure 1. The Tai Mo Shan (TMS) and Tsuen Wan (TW) sampling sites and the surrounding environment in Hong Kong.

ACPD
15, 22597–22636, 2015

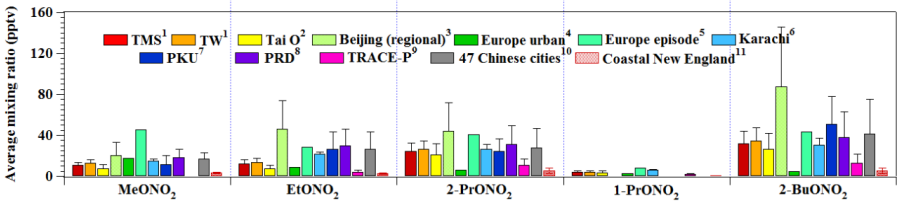

Figure 2. Comparison of $RONO_2$ in different locations. Data collected by UCI before 2008 (PRD and TRACE-P) were adjusted to UCI's new calibration scale to permit direct comparison (see text for details about the new calibration). [1] This study, September–November 2010. [2] Rural site, August 2001–December 2002 (Simpson et al., 2006). [3] Urban site, 2009–2011 (Wang et al., 2013). [4] Urban sites, April–May 2004 (Worton et al., 2010). [5] Urban sites, April–May 2004 (Worton et al., 2010). [6] Coastal site, December 1998–January 1999 (Barletta et al. 2002). [7] Urban site, August–September 2011 and December 2011–January 2012 (Wang et al., 2013). [8] Regional background sites, September 2009 (Wang et al., 2013). [9] Aircraft measurement, February–April 2001 (Simpson et al., 2003). [10] Regional background sites, July 2010 (Wang et al., 2009). [11] Coastal site, January–February and June–August 2002, July–August 2004.

ACPD
15, 22597–22636, 2015

Figure 3. Time series of $MeONO_2$, $EtONO_2$, 1-$PrONO_2$, 2-$PrONO_2$ and 2-$BuONO_2$ measured at TMS (purple) and TW (red) in 2010. The O_3 episode days are highlighted in bold on the *x* axis. Note that the *x* axis is discontinuous.

ACPD
15, 22597–22636, 2015

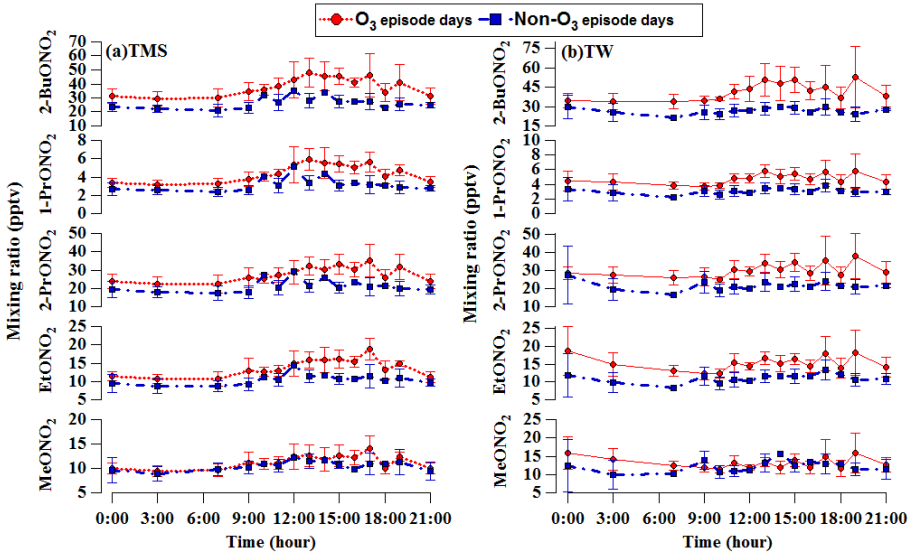

Figure 4. Diurnal variations of $RONO_2$ on O_3 and non-O_3 episode days at **(a)** TMS and **(b)** TW.

ACPD
15, 22597–22636, 2015

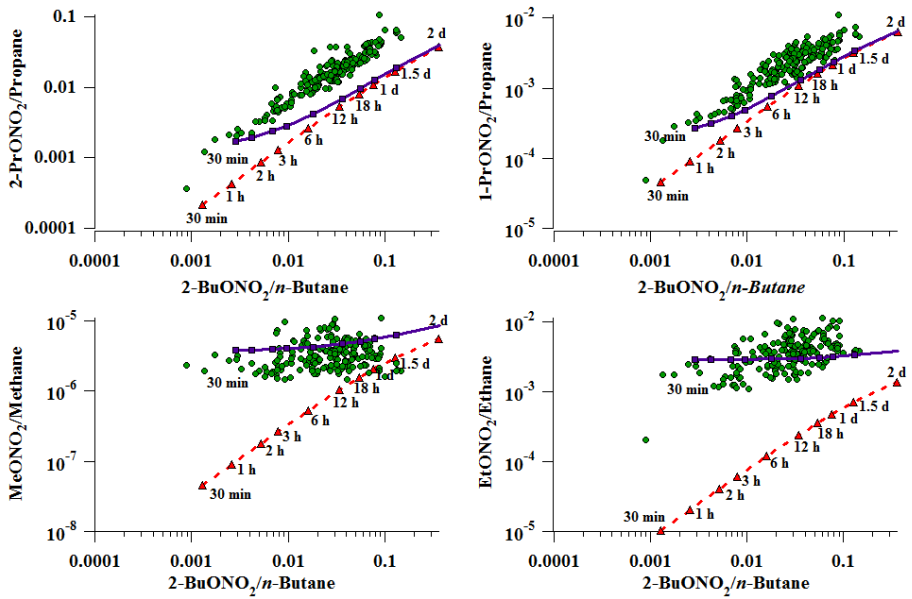

Figure 5. The relationships of C_1–C_3 $RONO_2$/RH vs. 2-$BuONO_2$/*n*-butane at Tai O. The red dash and purple solid curves were predicted based on zero initial levels (pure photochemical curves) and initial levels with the lowest ratios of $RONO_2$/RH at 07:00 LT (background initial ratios curves), respectively.

ACPD
15, 22597–22636, 2015

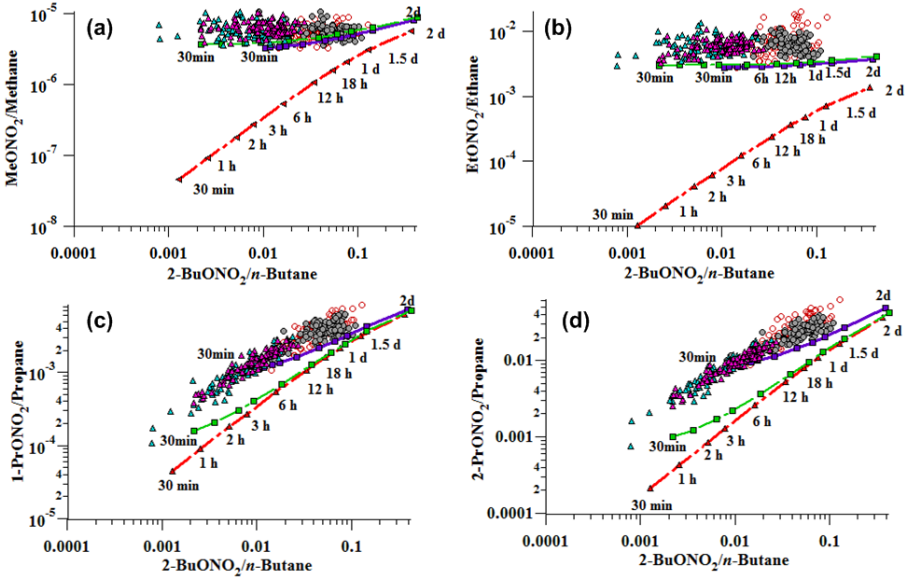

Figure 6. Relationships of C_1–C_3 $RONO_2$/RH to 2-$BuONO_2$/*n*-butane at TMS and TW. The red dashed curves were predicted based on zero initial concentrations of RH and $RONO_2$ (pure photochemical curves, PP) at both sites, while the purple and green solid curves were predicted based on non-zero initial levels at TMS and TW, respectively (background initial ratio, BIR), with the lowest ratios of $RONO_2$/RH from 00:00 to 07:00 LT. The solid gray circles and empty red circles were the measured ratios for samples collected on O_3 and non-O_3 episode days at TMS, respectively, while the pink and blue solid triangles were the measured ratios for samples collected on O_3 and non-O_3 episode days at TW, respectively.

ACPD
15, 22597–22636, 2015

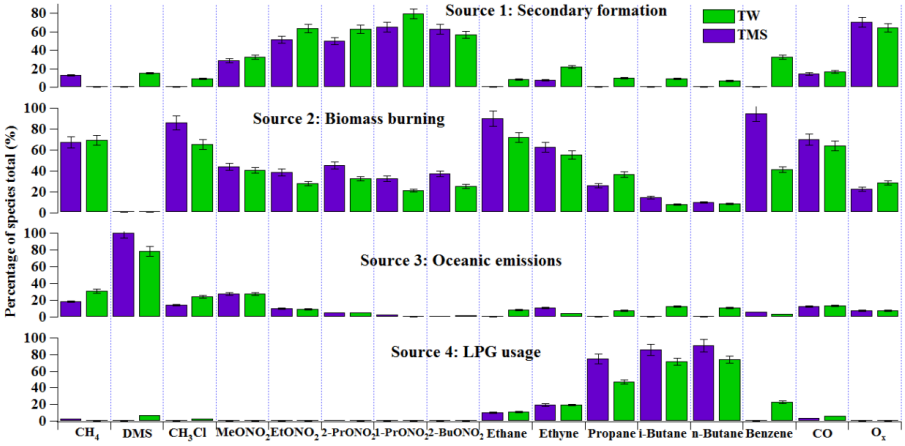

Figure 7. Explained variations of species in the identified sources extracted by the PMF model.

ACPD
15, 22597–22636, 2015